Robust Oscillation Damping Control for Multi-VSG Microgrids Under Line Impedance Uncertainties

Yuping Zhang[1], Yunyun Xie[1,*], Sheng Cai[1], Lei Yu[1], Jie Zhu[1], Chenguang Qiu[2]
[1]School of Automation, Nanjing University of Science and Technology, Nanjing 210094, China
E-mail: zyp@njust.edu.cn, yunyun_xie@njust.edu.cn, njustauto_cs@163.com, 467692958@qq.com, 2425441990@qq.com
[2]State Grid Jiangsu Electric Power Co., Ltd, Nanjing 210094, China
E-mail: cgqiu@hotmail.com

***Abstract*—Parallel virtual synchronous generators (VSGs) with parameter mismatches are prone to power oscillation, necessitating additional damping control for stabilization. However, most existing damping strategies are predicated on an assumption of constant line impedance, and therefore lack robustness against realistic impedance variations. To overcome this limitation, this paper develops a robust damping control for multi-VSG microgrids that explicitly accounts for line impedance uncertainties. The designed controller employs a high-pass filter structure to extract the oscillatory component of the VSG output power for suppression. Moreover, the controller parameters are optimized by minimizing the structured singular value of the perturbed microgrid model to maximize its robust stability margin against uncertainties. Simulation results demonstrate that the proposed controller effectively enhances system damping under diverse line impedance conditions.**

***Index Terms*—Power oscillation suppression, robust damping control, virtual synchronous generators, microgrids.**

I. Introduction

The widespread deployment of power electronic inverters to integrate renewable resources introduces challenges to power system frequency stability [1]. As a countermeasure, virtual synchronous generator (VSG) control has been developed for inverter-based sources to provide inertia and frequency support capability [2]. Nevertheless, in microgrids with multiple VSGs, mismatched control or impedance parameters among units can lead to power oscillation. This issue may jeopardize the normal operation of VSGs due to their inherently limited over-current capability, highlighting the necessity to explore damping control strategies to suppress the oscillation [3].

Previous power oscillation suppression strategies primarily involved adjusting VSG control parameters to enhance system damping. For example, in [4], an adaptive droop coefficient adjustment strategy was proposed to maintain adequate damping upon detecting power oscillation. In [5], an alternating inertia scheme was introduced to suppress power oscillation by adaptively selecting virtual inertia values during different oscillation phases. Besides, studies have found that properly designed virtual impedances can effectively suppress power oscillation among parallel VSGs [6], [7]. However, the adjustment of VSG control parameters would inevitably affect the frequency control performance in both transient and steady-states, as well as the accuracy of power sharing.

To avoid these adverse effects, considerable effort has been devoted to incorporating additional damping controllers into the VSG power loop. In [8] and [9], a damping controller that uses both power output and angular frequency feedback was proposed to mitigate power oscillation among parallel VSGs. In [10], a decentralized mutual damping strategy was presented for multi-VSG systems which achieves oscillation suppression without communication. For more specialized applications, a simplified power system stabilizer was developed in [11] to mitigate power oscillation in grid-forming wind-storage hybrid systems. The study in [12] proposed a coefficient-decoupling strategy that enhances sub-synchronous oscillation damping while reducing the power rating requirement of energy storage. Besides, a fractional-order damping controller was introduced in [13] to provide effective oscillation damping and maintain the designed inertial response characteristics of VSGs.

Although the aforementioned approaches have demonstrated enhanced damping performance, they are typically designed based on constant line impedance parameters. However, these parameters can deviate from their nominal values in practice due to factors such as temperature fluctuations, line aging, and network reconfiguration, thereby undermining the performance of damping controllers designed for fixed parameters. Consequently, it is essential to develop robust damping strategies for ensuring system stability under such parametric variations.

To address this challenge, a robust damping control strategy that explicitly accounts for line impedance uncertainties is proposed to suppress power oscillation in multi-VSG microgrids. First, a high-pass filter-based damping controller is utilized to extract the oscillatory component from the VSG output power, which is subtracted from the original power signal to mitigate the oscillation. Furthermore, a perturbed microgrid model is built using linear fractional transformation (LFT) to model line impedance uncertainties. Finally, the controller parameters are designed by solving an optimization problem that minimizes the structured singular value (SSV) of the perturbed system, enhancing its robust stability margin. In contrast to existing strategies, the proposed controller sustains adequate damping across a wider range of line impedance uncertainties.

This paper is structured as follows. Section II introduces the multi-VSG microgrid model. Section III presents the proposed

This work was supported by the National Key Research and Development Program of China under Grants 2024YFB2408900.

979-8-3315-8138-1

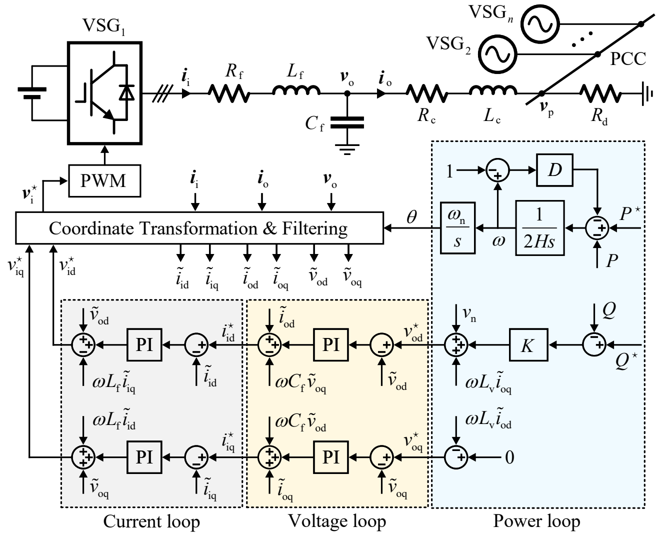

Fig. 1. Topology of the studied microgrid and VSG control diagram.

robust damping controller. Simulation studies are presented in Section IV, and conclusions are drawn in Section V.

II. Modeling of Multi-VSG Microgrids

Fig. 1 illustrates the topology of a microgrid with multiple VSGs and the VSG control diagram. Each VSG is composed of an ideal DC voltage source, an inverter, and an LC filter, and is connected to the point of common coupling (PCC) via a line impedance. The detailed model of the VSG is established in the dq rotating reference frame with a per-unit representation. For notational simplicity, we define:

$$\boldsymbol{h}_{\mathrm{dq}} \triangleq \begin{bmatrix} h_{\mathrm{d}} & h_{\mathrm{q}} \end{bmatrix}^\top, \ \boldsymbol{h}_{\mathrm{qd}} \triangleq \begin{bmatrix} h_{\mathrm{q}} & -h_{\mathrm{d}} \end{bmatrix}^\top \tag{1}$$

where $h \in \{v, i, e, w, z\}$ represents voltage, current, the state of a proportional-integral (PI) regulator and the fictitious input and output introduced in uncertainty modeling, respectively. In addition, the notations $h^\star$ and $\tilde{h}$ represent the reference and filtered measurement of h, respectively.

A. Virtual Synchronous Generator Model

The dynamics of the VSG main circuits can be described by the following set of equations for filter current, filter voltage, and line current:

$$L_{\mathrm{f}}\dot{\boldsymbol{i}}_{\mathrm{idq}} = \boldsymbol{v}_{\mathrm{idq}} - \boldsymbol{v}_{\mathrm{odq}} - R_{\mathrm{f}}\boldsymbol{i}_{\mathrm{idq}} + \omega L_{\mathrm{f}}\boldsymbol{i}_{\mathrm{iqd}} \tag{2}$$

$$C_{\mathrm{f}}\dot{\boldsymbol{v}}_{\mathrm{odq}} = \boldsymbol{i}_{\mathrm{idq}} - \boldsymbol{i}_{\mathrm{odq}} + \omega C_{\mathrm{f}}\boldsymbol{v}_{\mathrm{oqd}} \tag{3}$$

$$L_{\mathrm{c}}\dot{\boldsymbol{i}}_{\mathrm{odq}} = \boldsymbol{v}_{\mathrm{odq}} - \boldsymbol{v}_{\mathrm{pdq}} - R_{\mathrm{c}}\boldsymbol{i}_{\mathrm{odq}} + \omega L_{\mathrm{c}}\boldsymbol{i}_{\mathrm{oqd}} \tag{4}$$

where i_{i} and v_{o} are the filter current and voltage; i_{o} is the line current; v_{p} is the PCC voltage; ω is the angular frequency; L_{f} and C_{f} are the filter inductance and capacitance; R_{c} and L_{c} are the line resistance and inductance.

The VSG control strategy consists of power, voltage, and current loops. The power loop determines the output voltage reference, which is mathematically described by:

$$2H\dot{\omega} = P^\star - P - D\left(\omega - \omega_{\mathrm{n}}\right) \tag{5}$$

$$\dot{\theta} = \omega\omega_{\mathrm{b}} \tag{6}$$

$$v_{\mathrm{od}}^\star = v_{\mathrm{n}} - K\left(Q^\star - Q\right), \ v_{\mathrm{oq}}^\star = 0 \tag{7}$$

$$P = \tilde{v}_{\mathrm{od}}\tilde{i}_{\mathrm{od}} + \tilde{v}_{\mathrm{oq}}\tilde{i}_{\mathrm{oq}}, \ Q = \tilde{v}_{\mathrm{oq}}\tilde{i}_{\mathrm{od}} - \tilde{v}_{\mathrm{od}}\tilde{i}_{\mathrm{oq}} \tag{8}$$

where H is the virtual inertia constant; D and K are the droop coefficients for frequency and voltage control; ω_{n} and v_{n} are the nominal angular frequency and output voltage; ω_{b} is the base angular frequency; P and Q are the active and reactive power outputs, respectively.

The output voltage reference is sent to the inner voltage and current controllers for execution, which can be expressed as:

$$\boldsymbol{i}_{\mathrm{idq}}^\star = \tilde{\boldsymbol{i}}_{\mathrm{odq}} - \omega C_{\mathrm{f}}\tilde{\boldsymbol{v}}_{\mathrm{oqd}} + k_{\mathrm{pv}}\dot{\boldsymbol{e}}_{\mathrm{vdq}} + k_{\mathrm{iv}}\boldsymbol{e}_{\mathrm{vdq}} \tag{9}$$

$$\boldsymbol{v}_{\mathrm{idq}}^\star = \tilde{\boldsymbol{v}}_{\mathrm{odq}} - \omega L_{\mathrm{f}}\tilde{\boldsymbol{i}}_{\mathrm{oqd}} + k_{\mathrm{pc}}\dot{\boldsymbol{e}}_{\mathrm{cdq}} + k_{\mathrm{ic}}\boldsymbol{e}_{\mathrm{cdq}} \tag{10}$$

$$\dot{\boldsymbol{e}}_{\mathrm{vdq}} = \boldsymbol{v}_{\mathrm{odq}}^\star - \tilde{\boldsymbol{v}}_{\mathrm{odq}} + \omega L_{\mathrm{v}}\tilde{\boldsymbol{i}}_{\mathrm{oqd}}, \ \dot{\boldsymbol{e}}_{\mathrm{cdq}} = \boldsymbol{i}_{\mathrm{idq}}^\star - \tilde{\boldsymbol{i}}_{\mathrm{idq}} \tag{11}$$

$$T_{\mathrm{f}}\dot{\tilde{\boldsymbol{i}}}_{\mathrm{idq}} = \boldsymbol{i}_{\mathrm{idq}} - \tilde{\boldsymbol{i}}_{\mathrm{idq}}, \ T_{\mathrm{f}}\dot{\tilde{\boldsymbol{i}}}_{\mathrm{odq}} = \boldsymbol{i}_{\mathrm{odq}} - \tilde{\boldsymbol{i}}_{\mathrm{odq}} \tag{12}$$

$$T_{\mathrm{f}}\dot{\tilde{\boldsymbol{v}}}_{\mathrm{odq}} = \boldsymbol{v}_{\mathrm{odq}} - \tilde{\boldsymbol{v}}_{\mathrm{odq}} \tag{13}$$

where two PI regulators are used in (9) and (10) to compute the references for the inverter current and voltage, respectively. In (11), the voltage reference from the power loop is adjusted by subtracting the voltage drop across the virtual impedance L_{v}. Equations (12) and (13) represent the filtering of the current and voltage measurements, where T_{f} is the filter time constant.

B. Microgrid model

The aforementioned model for a single VSG is established in its local dq reference frame. To construct the overall model of a microgrid with n VSGs, an interface model is employed to transform the variables from the reference frame of the i-th VSG to that of the j-th VSG, as expressed by:

$$\boldsymbol{h}_{\mathrm{dq}i}^{(j)} = \begin{bmatrix} \cos\left(\theta_j - \theta_i\right) & \sin\left(\theta_j - \theta_i\right) \\ -\sin\left(\theta_j - \theta_i\right) & \cos\left(\theta_j - \theta_i\right) \end{bmatrix} \boldsymbol{h}_{\mathrm{dq}i}^{(i)} \tag{14}$$

In a unified dq reference frame, the nodal current equation at the PCC can be obtained as follows:

$$\boldsymbol{i}_{\mathrm{pdq}} = \sum_{i=1}^{n} \boldsymbol{i}_{\mathrm{odq}i} \tag{15}$$

where i_{p} is the load current. To simplify the modeling, in this work, the load is considered purely resistive and denoted as R_{p}, allowing the PCC voltage to be expressed as an explicit function of the load current:

$$\boldsymbol{v}_{\mathrm{pdq}} = R_{\mathrm{d}}\boldsymbol{i}_{\mathrm{pdq}} \tag{16}$$

Integrating the component models from (2) to (16) yields the overall microgrid model, which is formulated as the following compact state-space form:

$$\dot{\boldsymbol{x}}_{\mathrm{mg}} = \boldsymbol{f}_{\mathrm{mg}}\left(\boldsymbol{x}_{\mathrm{mg}}\right) \tag{17}$$

where $\boldsymbol{x}_{\mathrm{mg}} = [\boldsymbol{x}_1, \boldsymbol{x}_2, \ldots, \boldsymbol{x}_n]^\top$ represents the integrated state vector of the microgrid, formed by stacking the state vectors of all VSGs. The state vector of a single VSG is defined as:

$$\boldsymbol{x} = \left[\boldsymbol{i}_{\mathrm{idq}}, \boldsymbol{v}_{\mathrm{odq}}, \boldsymbol{i}_{\mathrm{odq}}, \omega, \theta, \boldsymbol{e}_{\mathrm{vdq}}, \boldsymbol{e}_{\mathrm{cdq}}, \tilde{\boldsymbol{i}}_{\mathrm{idq}}, \tilde{\boldsymbol{v}}_{\mathrm{odq}}, \tilde{\boldsymbol{i}}_{\mathrm{odq}}\right]^\top \tag{18}$$

979-8-3315-8138-1

III. Robust Power Oscillation Damping Control

In this section, the modeling of line impedance uncertainty in the microgrid and the design of a power oscillation damping controller are introduced. Furthermore, a controller parameter optimization model, which aims to minimize the SSV of the perturbed microgrid model, is formulated to enhance system robustness against line impedance uncertainties.

A. Modeling of Line Impedance Uncertainty

Given that the inductive reactance typically dominates both the line impedance and the current dynamics, this work focuses on the uncertainty in line inductance, which is modeled as:

$$L_{\mathrm{c}} = L_{\mathrm{c0}}\left(1+\beta\delta\right) \tag{19}$$

where L_{c0} is the nominal inductance, δ denotes the normalized uncertainty perturbation, and β scales its magnitude.

Substituting the uncertain inductance model (19) into the original line current equation (4), we obtain:

$$\dot{\boldsymbol{i}}_{\mathrm{odq}} = \frac{1}{L_{\mathrm{c0}}\left(1+\beta\delta\right)}\left(\boldsymbol{v}_{\mathrm{odq}} - \boldsymbol{v}_{\mathrm{pdq}} - R_{\mathrm{c}}\boldsymbol{i}_{\mathrm{odq}}\right) + \omega\boldsymbol{i}_{\mathrm{oqd}} \tag{20}$$

Equation (20) shows that the inductance uncertainty results in a nonlinear current model. Thus, the uncertainty cannot be directly separate from the nominal model. To address this, the LFT technique is used to decompose the uncertain object into fixed certain and normalized uncertain parts as follows:

$$\frac{1}{L_{\mathrm{c0}}\left(1+\beta\delta\right)} = \mathcal{F}_l\left(\begin{bmatrix} L_{\mathrm{c0}}^{-1} & -\beta L_{\mathrm{c0}}^{-1} \\ 1 & -\beta \end{bmatrix}, \delta\right) \tag{21}$$

where $\mathcal{F}_l$ denotes the lower LFT formalism.

By introducing a fictitious input w and output z for the uncertain object, the nonlinear uncertain model (20) can be transformed into:

$$\dot{\boldsymbol{i}}_{\mathrm{odq}} = \frac{1}{L_{\mathrm{c0}}}\left(\boldsymbol{v}_{\mathrm{odq}} - \boldsymbol{v}_{\mathrm{pdq}} - R_{\mathrm{c}}\boldsymbol{i}_{\mathrm{odq}} - \beta\boldsymbol{w}_{\mathrm{dq}}\right) + \omega\boldsymbol{i}_{\mathrm{oqd}} \tag{22}$$

$$\boldsymbol{z}_{\mathrm{dq}} = \boldsymbol{v}_{\mathrm{odq}} - \boldsymbol{v}_{\mathrm{pdq}} - R_{\mathrm{c}}\boldsymbol{i}_{\mathrm{odq}} - \beta\boldsymbol{w}_{\mathrm{dq}} \tag{23}$$

where (22) describes the nominal current model, while (23) defines the uncertainty channel. The normalized uncertainty δ is embedded via a feedback interconnection $w = \delta z$.

B. Damping Controller Design

A high-pass filter is used as the damping controller, which is incorporated into each VSG in a decentralized manner, to suppress the power oscillation among parallel VSGs.

The controller synthesizes a damping power component to mitigate the oscillatory power component [11]. Accordingly, the original VSG rotor motion equation (5) is rewritten as:

$$2H\dot{\omega} = P^{\star} - P - D\left(\omega - \omega_{\mathrm{n}}\right) - P_{\mathrm{c}} \tag{24}$$

where P_{c} denotes the damping power component synthesized by the high-pass filter, which can be expressed as:

$$\begin{cases} \tau\dot{x}_{\mathrm{c}} = P - x_{\mathrm{c}} \\ P_{\mathrm{c}} = \kappa\left(P - x_{\mathrm{c}}\right) \end{cases} \tag{25}$$

where κ and τ are the filter gain and time constant.

C. Controller Parameter Optimization

By incorporating both the line inductance uncertainty and the damping controller dynamics, the original microgrid model (17) are extended to the following augmented uncertain model:

$$\begin{cases} \dot{\boldsymbol{x}}_{\mathrm{aug}} = \boldsymbol{f}_{\mathrm{aug}}\left(\boldsymbol{x}_{\mathrm{aug}}, \boldsymbol{w}_{\mathrm{aug}}\right) \\ \boldsymbol{z}_{\mathrm{aug}} = \boldsymbol{g}_{\mathrm{aug}}\left(\boldsymbol{x}_{\mathrm{aug}}, \boldsymbol{w}_{\mathrm{aug}}\right) \end{cases} \tag{26}$$

where $\boldsymbol{x}_{\mathrm{aug}} = [\boldsymbol{x}_{\mathrm{mg}}, \boldsymbol{x}_{\mathrm{c}}]^{\top}$, $\boldsymbol{x}_{\mathrm{c}} = [x_{\mathrm{c}1}, x_{\mathrm{c}2}, \ldots, x_{\mathrm{c}n}]^{\top}$, $\boldsymbol{w}_{\mathrm{aug}} = [\boldsymbol{w}_{\mathrm{dq}1}, \boldsymbol{w}_{\mathrm{dq}2}, \ldots, \boldsymbol{w}_{\mathrm{dq}n}]^{\top}$, $\boldsymbol{z}_{\mathrm{aug}} = [\boldsymbol{z}_{\mathrm{dq}1}, \boldsymbol{z}_{\mathrm{dq}2}, \ldots, \boldsymbol{z}_{\mathrm{dq}n}]^{\top}$.

The inductance perturbations are assembled into a diagonal matrix $\boldsymbol{\Delta} = \mathrm{diag}\left(\delta_1\boldsymbol{I}_2, \delta_2\boldsymbol{I}_2, \ldots, \delta_n\boldsymbol{I}_2\right)$, where $\boldsymbol{I}_2$ denotes the second-order identity matrix.

To analyze the system robustness, the nonlinear model (26) is linearized around its equilibrium point, which can be further expressed as the following linear model:

$$\begin{cases} \dot{\boldsymbol{x}}_{\mathrm{aug}} = \boldsymbol{A}\boldsymbol{x}_{\mathrm{aug}} + \boldsymbol{B}\boldsymbol{w}_{\mathrm{aug}} \\ \boldsymbol{z}_{\mathrm{aug}} = \boldsymbol{C}\boldsymbol{x}_{\mathrm{aug}} + \boldsymbol{D}\boldsymbol{w}_{\mathrm{aug}} \end{cases} \tag{27}$$

where $\boldsymbol{A}$, $\boldsymbol{B}$, $\boldsymbol{C}$, and $\boldsymbol{D}$ are the linearized system matrices.

The transfer function matrix of $\boldsymbol{w}$ to $\boldsymbol{z}$ of the system (27) can be obtained using the following upper LFT:

$$\boldsymbol{G}\left(s\right) = \mathcal{F}_u\left(\begin{bmatrix} \boldsymbol{A} & \boldsymbol{B} \\ \boldsymbol{C} & \boldsymbol{D} \end{bmatrix}, \frac{1}{s}\boldsymbol{I}\right) = \boldsymbol{C}\left(s\boldsymbol{I} - \boldsymbol{A}\right)^{-1}\boldsymbol{B} + \boldsymbol{D} \tag{28}$$

Furthermore, the SSV of the closed system $\boldsymbol{G}$ with respect to the uncertainty block $\boldsymbol{\Delta}$ can be calculated by:

$$\mu_{\boldsymbol{\Delta}}\left(\boldsymbol{G}\right) = \frac{1}{\min\left\{\sigma_{\max}\left(\boldsymbol{\Delta}\right) \mid \det\left(\boldsymbol{I} - \boldsymbol{G}\boldsymbol{\Delta}\right) = 0\right\}} \tag{29}$$

where $\sigma_{\max}\left(\boldsymbol{\Delta}\right)$ denotes the maximum singular value of the uncertainty matrix $\boldsymbol{\Delta}$. The value of $\mu_{\Delta}(\boldsymbol{G})$ quantifies system robustness: a smaller μ implies the system can tolerate larger perturbations without losing stability. Consequently, designing a robust damping controller for maximum perturbation tolerance is equivalent to an optimization problem of minimizing the value of μ.

With the controller structure fixed in (25), the design task becomes a controller parameter optimization problem, which can be achieved by solving the following model:

$$\min_{\boldsymbol{\chi}} \quad J\left(\boldsymbol{\chi}\right) = \mu_{\boldsymbol{\Delta}}\left(\boldsymbol{G}\left(s, \boldsymbol{\chi}\right)\right) \tag{30a}$$

$$\text{s.t.} \quad \boldsymbol{\chi}_{\min} \preceq \boldsymbol{\chi} \preceq \boldsymbol{\chi}_{\max} \tag{30b}$$

$$\boldsymbol{\lambda}\left(\boldsymbol{A}\left(\boldsymbol{\chi}\right)\right) \subseteq \mathcal{D} \tag{30c}$$

$$\mu_{\boldsymbol{\Delta}}\left(\boldsymbol{G}\left(s, \boldsymbol{\chi}\right)\right) < 1 \tag{30d}$$

where $\boldsymbol{\chi} = [\kappa_1, \tau_1, \kappa_2, \tau_2, \ldots, \kappa_n, \tau_n]$ denotes the parameter vector to be optimized, bounded between $\boldsymbol{\chi}\mathrm{min}$ and $\boldsymbol{\chi}\mathrm{max}$, J is the objective function, $\sigma(\boldsymbol{A}(\boldsymbol{\chi}))$ represents the spectrum of the nominal closed-loop system matrix, and $\mathcal{D}$ is a predefined region in the complex plane.

The constraint (30c) places all eigenvalues of the nominal system within the desired complex region, preserving adequate oscillation damping. Meanwhile, the constraint (30d) ensures robust stability of the uncertain system across a given range of line impedance uncertainties.

979-8-3315-8138-1

TABLE I
CONTROL PARAMETERS OF THE SIMULATED SYSTEM

Par.	Val.	Unit	Par.	Val.	Unit
H_1/H_2	3/5	p.u.	$k_{\mathrm{pv1}}/k_{\mathrm{pv2}}$	1/1	–
D_1/D_2	40/40	p.u.	$k_{\mathrm{iv1}}/k_{\mathrm{iv2}}$	2/2	–
K_1/K_2	0.05/0.05	p.u.	$k_{\mathrm{pc1}}/k_{\mathrm{pc2}}$	1/1	–
$L_{\mathrm{v1}}/L_{\mathrm{v2}}$	0.05/0.05	p.u.	$k_{\mathrm{ic1}}/k_{\mathrm{ic2}}$	5/5	–
κ_1/κ_2	3.55/3.01	–	τ_1/τ_2	0.009/0.011	–

The abstract nature of the SSV and eigenvalue, which lack explicit expressions in the decision variables, precludes the use of analytical solution algorithms to deal with the optimization problem (30). Therefore, the genetic algorithm, which does not rely on analytical model gradients, is adopted to heuristically seek the optimal control parameters.

IV. SIMULATION STUDIES

This section presents a dynamic simulation of a two-VSGs microgrid to evaluate the effectiveness and robustness of the proposed oscillation suppression strategy. The capacity of each VSG is 500 kW. The nominal frequency and line voltage of the microgrid are 50 Hz and 380 V, respectively. The filter inductance, resistance and capacitance of each VSG are both set as 0.15, 0.003 and 0.65 p.u., respectively. Additional parameters of the simulated system are summarized in Table I.

For line impedance uncertainty modeling, the resistance of both lines is set to 0.01 p.u., while the inductances for VSG1 and VSG2 are set to 0.05 p.u. and 0.1 p.u., respectively, each with a relative uncertainty weight of 50%. For controller comparison, two parameter sets are considered: one obtained using a conventional damping strategy and the other via the proposed approach. The conventional strategy optimizes parameters based on the damping ratio of dominant oscillation modes, whereas the proposed method solves an optimization problem that maximizes the robust stability margin under line inductance uncertainty.

A. Performance under 10% Line Impedance Reduction

In this scenario, the system is simulated with a minor 10% reduction in line inductance relative to the nominal value to evaluate the oscillation suppression performance of the proposed robust controller against the conventional controller from [11]. Both controllers are tested under this slightly perturbed impedance condition, and their performance is assessed based on overshoot magnitude, oscillation period, and decay rate of the active power response following a load step change. At t = 5 s, the load resistance is decreased from 2.5 p.u. to 1.25 p.u., while all other parameters remain unchanged. The active power outputs of the VSGs under the conventional and proposed controllers are compared in Fig. 2 and Fig. 3, respectively.

Under this slight impedance deviation, both control methods maintain the ability to suppress oscillations following the

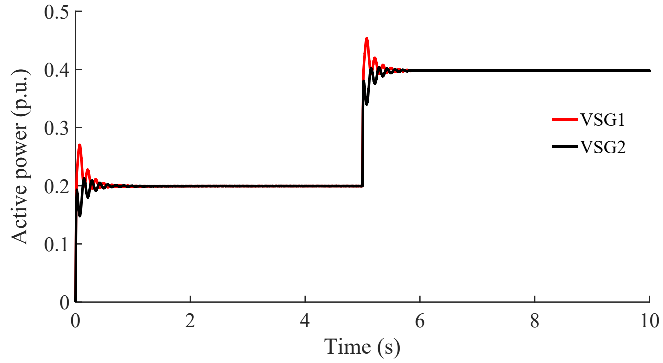

Fig. 2. Active power of VSGs under conventional damping control

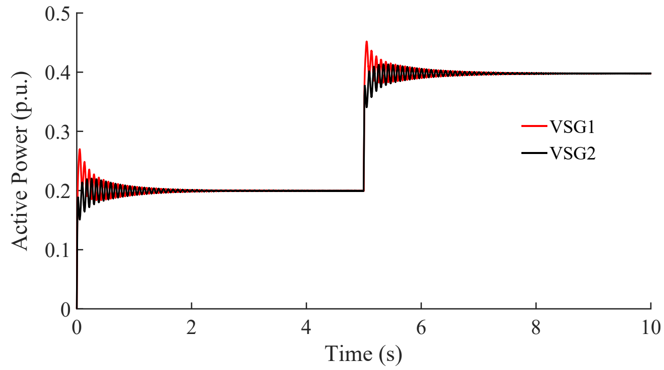

Fig. 3. Active power of VSGs under robust damping control

disturbance, with power deviations limited to approximately 0.05 p.u. in both cases. The conventional controller achieves stabilization within about 0.8 s, still outperforming the robust controller, which requires nearly 2 s to settle. This result aligns with expectations: the conventional controller, optimized for the nominal system, continues to deliver superior dynamic performance under minor parameter variations. In contrast, the robust controller, designed to maintain stability across a wider range of impedance values, exhibits a more conservative response even under this modest impedance reduction. This behavior illustrates the inherent trade-off between optimal damping performance at specific operating points and consistent robustness across a range of conditions.

B. Performance under 50% Line Impedance Reduction

This scenario considers the maximum uncertainty range, where the line inductance of both VSGs are reduced by 50% from their nominal values. The system is subjected to the same load disturbance as in previous tests to evaluate oscillation suppression performance under extreme parameter variation. The resulting active power responses of the conventional and proposed controllers are provided in Fig. 4 and Fig. 5, respectively. Under such a severe impedance deviation, the conventional controller, which was optimized specifically for the nominal system parameters, fails to maintain system stability and leads to sustained power oscillations. By contrast,

979-8-3315-8138-1

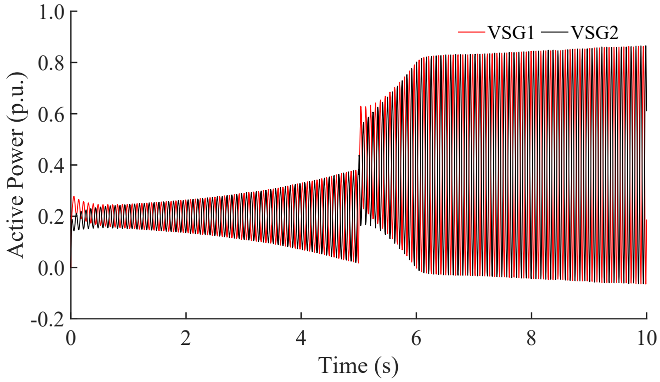

Fig. 4. Active power of VSGs under conventional damping control

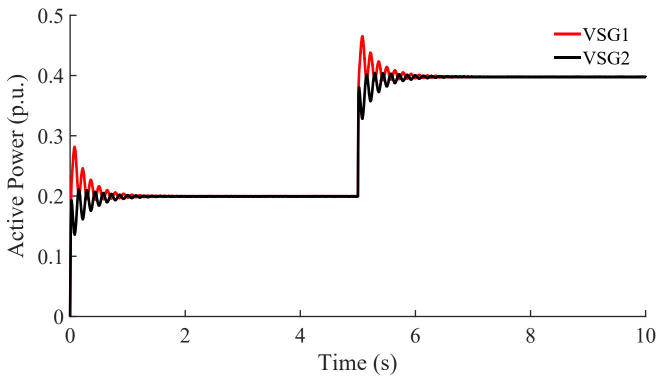

Fig. 5. Active power of VSGs under robust damping control

the proposed robust controller successfully suppresses the oscillations and restores system stability within 1 s.

This marked difference in performance stems from the fundamental design principles of the two methods: the conventional approach seeks optimal dynamic performance at the nominal operating point, whereas the robust method explicitly accounts for a predefined range of impedance uncertainty. As a result, the proposed controller preserves consistent damping capability across varying line impedance conditions, demonstrating adaptability and enhanced robustness in the presence of substantial parameter uncertainties. These results underscore the practical value of the robust damping strategy for real-world microgrid applications, where system parameters may deviate significantly from their nominal values.

V. Conclusions

This paper proposes a robust damping control strategy that maintains effective performance under line impedance uncertainty. The controller parameters are optimized by minimizing the SSV of the perturbed system to maximize its robust stability margin. Simulation results verify that the proposed robust damping controller effectively suppresses power oscillations and ensures stability within the predefined uncertainty range. However, this robustness is achieved at the cost of sub-optimal dynamic performance under nominal conditions, revealing a inherent trade-off between robustness and rapid oscillation suppression. Therefore, adaptive damping control strategies, capable of dynamically adjusting parameters to balance robustness and damping under different operating conditions, are worthy to be further investigated.

References

[1] D. Pattabiraman, R. H. Lasseter., and T. M. Jahns, "Comparison of grid following and grid forming control for a high inverter penetration power system," in *Proc. IEEE Power Energy Soc. General Meeting (PESGM)*, 2018, pp. 1–5.

[2] B. Kroposki, B. Johnson, Y. Zhang, V. Gevorgian, P. Denholm, B.-M. Hodge, and B. Hannegan, "Achieving a 100% renewable grid: Operating electric power systems with extremely high levels of variable renewable energy," *IEEE Power Energy Mag.*, vol. 15, no. 2, pp. 61–73, Mar. 2017.

[3] S. Fu, Y. Sun, L. Li, Z. Liu, H. Han, and M. Su, "Power oscillation suppression in multi-vsg grid by adaptive virtual impedance control," *IEEE Syst. J.*, vol. 16, no. 3, pp. 4744–4755, Sep. 2022.

[4] T. Shintai, Y. Miura, and T. Ise, "Oscillation damping of a distributed generator using a virtual synchronous generator," *IEEE Trans. Power Del.*, vol. 29, no. 2, pp. 668–676, Apr. 2014.

[5] J. Alipoor, Y. Miura, and T. Ise, "Power system stabilization using virtual synchronous generator with alternating moment of inertia," *IEEE Trans. Emerg. Sel. Topics Power Electron.*, vol. 3, no. 2, pp. 451–458, Jun. 2015.

[6] J. Liu, Y. Miura, H. Bevrani, and T. Ise, "Enhanced virtual synchronous generator control for parallel inverters in microgrids," *IEEE Trans. Smart Grid*, vol. 8, no. 5, pp. 2268–2277, Sep. 2017.

[7] Z. Shuai, W. Huang, Z. J. Shen, A. Luo, and Z. Tian, "Active power oscillation and suppression techniques between two parallel synchronverters during load fluctuations," *IEEE Trans. Power Electron.*, vol. 35, no. 4, pp. 4127–4142, Apr. 2020.

[8] M. Chen, D. Zhou, and F. Blaabjerg, "Active power oscillation damping based on acceleration control in paralleled virtual synchronous generators system," *IEEE Trans. Power Electron.*, vol. 36, no. 8, pp. 9501–9510, Aug. 2021.

[9] Z. Wang, Y. Chen, X. Li, Y. Xu, C. Luo, Q. Li, and Y. He, "Active power oscillation suppression based on decentralized transient damping control for parallel virtual synchronous generators," *IEEE Trans. Smart Grid*, vol. 14, no. 4, pp. 2582–2592, Jul. 2023.

[10] S. Fu, Y. Sun, L. Li, Z. Liu, H. Han, and M. Su, "Power oscillation suppression of multi-vsg grid via decentralized mutual damping control," *IEEE Trans. Ind. Electron.*, vol. 69, no. 10, pp. 10 202–10 214, Oct. 2022.

[11] Y. Zhang, Y. Xie, S. Cai, Q. Wu, H. Zhu, and Z. Xiang, "Coordinated control of grid-forming wind turbines and grid-forming energy storage systems for power system restoration," *IEEE Trans. Sustain. Energy*, vol. 16, no. 4, pp. 2812–2827, Oct. 2025.

[12] Z. Zhou, S. Pugliese, M. Langwasser, and M. Liserre, "Subsynchronous damping by battery storage system in grid-forming control," *IEEE Trans. Power Electron.*, vol. 39, no. 4, pp. 4173–4186, Apr. 2024.

[13] Y. Yu, Y. Guan, W. Kang, J. C. Vasquez, and J. M. Guerrero, "A generic inertial-response preserved active-damping control for grid-forming inverters emulating synchronous machines," *IEEE Trans. Ind. Electron.*, vol. 72, no. 6, pp. 5897–5905, Jun. 2025.